

Smooth Flow in Diamond: Atomistic Ductility and Electronic Conductivity

Chang Liu^①, Xianqi Song^②, Quan Li^{③,*}, Yanming Ma^{①,2} and Changfeng Chen^{④,†}

¹*State Key Laboratory of Superhard Materials, Key Laboratory of Automobile Materials of MOE, Department of Materials Science, and Innovation Center for Computational Physics Method and Software, Jilin University, Changchun 130012, China*

²*International Center of Future Science, Jilin University, Changchun 130012, China*

³*Department of Physics and Astronomy, University of Nevada, Las Vegas, Nevada 89154, USA*



(Received 1 July 2019; published 6 November 2019)

Diamond is the quintessential superhard material widely known for its stiff and brittle nature and large electronic band gap. In stark contrast to these established benchmarks, our first-principles studies unveil surprising intrinsic structural ductility and electronic conductivity in diamond under coexisting large shear and compressive strains. These complex loading conditions impede brittle fracture modes and promote atomistic ductility, triggering rare smooth plastic flow in the normally rigid diamond crystal. This extraordinary structural change induces a concomitant band gap closure, enabling smooth charge flow in deformation created conducting channels. These startling soft-and-conducting modes reveal unprecedented fundamental characteristics of diamond, with profound implications for elucidating and predicting diamond's anomalous behaviors at extreme conditions.

DOI: 10.1103/PhysRevLett.123.195504

Diamond is best known for its extremely stiff and brittle nature described by steep stress responses and abrupt cleavages under strain; also notable is its large electronic band gap spanning a wide optical spectrum. While extrinsic factors like defects may influence material performance, intrinsic stress responses and electronic properties of the pristine crystal set fundamental benchmarks that are essential to defining material behaviors and deciphering atomistic mechanisms. Such benchmarks can be well described by stress-strain relations and electronic band structures from first-principles calculations that provide key knowledge for elucidating mechanical and electronic properties [1,2]. Recent studies have generated rich insights for understanding uniaxially strained diamond and other strong solids [3–14] and unexpected strengthening effects in multiaxially strained iron [15] and covalent compounds [16–18]. However, material behaviors under complex strains remain largely unexplored, raising exciting prospects for breakthrough discoveries.

In this Letter, we report that shear strains under proper compression constraints cause a surprising structural softening, triggering an uncharacteristic ductile smooth flow in the usually very rigid diamond crystal. Analysis of associated bonding changes reveals that compression constraints prevent cleavage-type graphitization that commonly occurs in severely strained diamond and, instead, produces local bonding rearrangements via anomalously large angular variations that open new pathways for exceptional creeplike shear flow deformations. Remarkably, this structural flow process creates distinct charge-flow channels for electronic conduction, producing metallic diamond in an extended

strain range. These robust structural, mechanical and electronic behaviors under constrained shear strains are in stark contrast to traditional benchmarks of diamond, showcasing unprecedented soft-and-conducting modes that redefine this quintessential superhard and insulating solid. The present findings offer key insights for elucidating and predicting novel behaviors of diamond in a variety of extreme loading environments, e.g., in strained anvils, under indentation or wear conditions, or in planetary interiors.

First-principles calculations are well suited for capturing prominent phenomena and key mechanisms underlying diamond's stiff and brittle nature, since these intrinsic behaviors are dictated by local bonding characters at length scales suitable for such accurate computations. For example, calculated tensile stresses along major crystallographic directions elucidate the mechanism for the dominant brittle cleavage on the (111) planes [3], and computations of shear stresses identify the (111)[11-2] easy shear slip directions and the surprisingly anisotropic (111)[-1-12] shear stress response [4]. These and other studies [10–12] all find steep rises of stresses and load-bearing bond lengths in diamond in response to increasing strains, leading to abrupt brittle structural failures via graphitization. Here, we adopt established procedures [16,17] to compute and evaluate stress responses of diamond under complex, previously unexplored strains in extreme loading environments [19], and we operate with the true (Cauchy) stresses.

Under [111] tensile strains, the main load-bearing bonds in diamond align in the direction of strain, making bond elongation the dominant deformation mode with minimal angular changes, and such restricted deformation produces

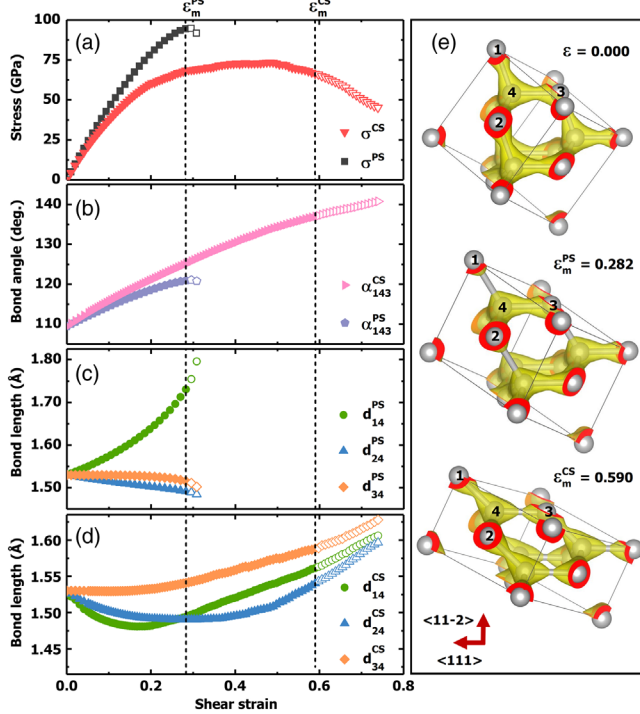


FIG. 1. (a) Stress response of diamond under (11-2)[111] pure shear (PS), σ_m^{PS} , and constrained shear (CS), σ_m^{CS} . A normal-to-shear stress ratio of 2.475 is maintained during CS, corresponding to biaxial stress fields under Vickers indentation. Data in open symbols indicate dynamic instability revealed by imaginary phonon modes (see Fig. S1 [19] for details). Maximal strains sustained by stably deformed diamond crystal under the PS and CS loadings are labeled as ϵ_m^{PS} and ϵ_m^{CS} , respectively, and marked by the two vertical dashed lines passing through all the panels. (b) Variation of the bond angle α_{143} between atom pairs 1-4 and 4-3 [see panel (e)] in deformed diamond crystal under the PS and CS strains. (c),(d) Variation of three key bond lengths, d_{14} , d_{24} , and d_{34} , in deformed diamond crystal under the PS and CS strains. (e) Structural snapshots at zero, maximal PS and CS strains, along with valence charge density showing changes in bonding strengths [3] (see Fig. S2 [19] for more details).

the lowest peak tensile stress that defines the well-known (111) easy cleavage planes in diamond [3]. This observation motivated us to probe shear deformations with the slip direction aligned with the [111] bonds. We have systematically examined stress-strain relations with the [111] slip in multiple shear planes under various loading conditions. Below, we present results under (11-2)[111] shear as a prototypical case and, later, will show that all the main findings remain robust under a wide range and variety of loading conditions.

We first assess diamond's stress response to (11-2)[111] pure shear (PS) strains, corresponding to nonzero shear stress in the specified direction and zero for all other five stress tensor components, and the obtained stress-strain relation is shown in Fig. 1(a), exhibiting behaviors typical for strong covalent solids. The responding stress rises to a

sharp-tipped peak where the main load-bearing 1-4 bonds in the [11-2] direction break [Fig. 1(c)], with nearly complete charge depletion at the maximal PS strain ϵ_m^{PS} [Fig. 1(e), middle] immediately preceding a catastrophic structural failure via graphitization [4,11,12]. Dynamic structural instability signified by the appearance of imaginary phonon modes develops as stress approaches the peak value, slightly shortening the deformation range, which has been observed in highly strained diamond, and the overall stress and structural responses under (11-2)[111] PS strains are similar to typical diamond behaviors under extensively studied (111)[11-2] PS and constrained shear (CS) strains [10–12,17].

In sharp contrast to the PS case, extraordinary structural deformation modes appear when diamond is subjected to CS strains with simultaneous presence of shear stress and compressive stress normal to the shear plane. Such biaxial stress environments are often encountered during wear and indentation processes and have produced novel strength enhancements in strong covalent solids [16–18,27,28]. Here, we examine structural responses under previously unexplored (11-2)[111] CS strains, maintaining a normal-to-shear stress ratio of 2.475, corresponding to the biaxial stress field in Vickers indentation [29,30], which is commonly employed to probe material hardness and deformation. We will show below, however, that our findings are robust and insensitive to this specific constraint. Under the CS strains, the stress response σ_m^{CS} [Fig. 1(a)] initially rises at a much slower rate compared to the PS case, and then stays essentially flat over a wide range of shear strain until dynamic instability sets in. Such creeplike deformation occurs in some metals and, more generally, in materials at elevated temperatures close to melting, but this kind of smooth structural flow without any temperature effect is unprecedented in strong covalent solids and is especially surprising in normally stiff and brittle diamond.

Analysis of structural data reveals a novel deformation mechanism in diamond under CS strains. The angle between the bonds connecting atoms pairs 1-4 and 4-3 increases from 109.5 degrees to 137.0 degrees at the largest dynamically stable strain [Fig. 1(b)], much smaller than 121.0 degrees under PS strains. This angular deformation mechanism is driven by the normal compression constraint, which hinders the elongation of the 1-4 bonds, thus, preventing the graphitization that occurs under the PS strains. This unusual mechanism has profound impacts on structural responses. First, it acts to accommodate rising strains through angular changes, thus, allowing a significantly reduced overall bond elongation under CS compared to PS [Figs. 1(c) and 1(d)], leading to a much reduced rate of stress increase with rising strains. Consequently, different bond lengths converge under CS to create a more sustainable deformation in diamond crystal, in contrast to the diverging bond-length changes under PS with an early structural failure due to the breaking of the singularly

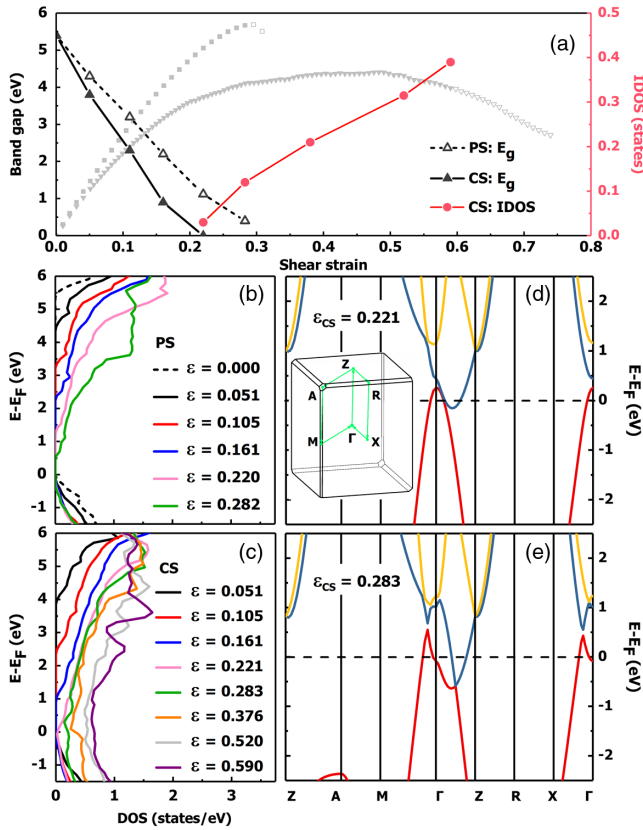


FIG. 2. (a) Electronic band gap E_g of deformed diamond along the PS and CS paths in Fig. 1(a) from first-principles calculations. Also shown are integrated density of states (IDOS) of electronic states within 0.3 eV on both sides of the Fermi energy under CS strains, as a measure of diamond’s ability for electronic conductivity. Stress-strain curves from Fig. 1(a) are shown in the background to offer a visible reference. (b),(c) Electronic density of states from Heyd-Scuseria-Ernzerhof hybrid functional calculations [19] at select PS and CS strains, highlighting band gap reduction under PS and full closure and metallization under CS. (d),(e) Electronic band structures revealing directional electron and hole conduction at CS strains of 0.22 and 0.28. Inset in (d) shows Brillouin zone with high-symmetry points.

stretched 1-4 bonds [Fig. 1(c)]. Second, the angular deformation also transfers the main load-bearing function from 1-4 bonds under PS strains to a more even distribution among three sets of bonds under the CS strains [Fig. 1(d)], further reducing the rate and extent of bond-length increases, resulting in a much slower stress rise. Third, increasing strains induce considerable but partial charge depletion on the main load-bearing 4-3 bonds aligned in the [111] shear slip direction [Fig. 1(e), bottom], weakening, yet still sustaining these bonds, which explains the extended flattening of the CS stress-strain curve despite the continuing bond elongations at large strains [Fig. 1(d)].

The anomalous structural deformation of diamond has profound impacts on its electronic properties. In Fig. 2(a), we present the calculated band gap of deformed diamond that decreases with rising strains under both PS and CS

loadings, which is opposite to the effect of uniform compression that enhances the band gap, while stress anisotropy causes certain gap suppression [31]. Here, under the PS strains, the band gap remains open up to the maximal strain ϵ_m^{PS} . In stark contrast, CS strains drive a band gap closure early on during the deformation process, leading to diamond’s metallization at surprisingly modest compressive stress of 146.5 GPa and shear stress 59.2 GPa. At increasing CS strains, an integrated density of states (IDOS) near the Fermi energy grows monotonically [Fig. 2(a)], reflecting CS strain enhanced metallic nature of deformed diamond, and the total electronic density of states at select strains under PS and CS strains are shown in Figs. 2(b) and 2(c). We have also tracked the evolution of the electronic band structure under increasing CS strains, and identified directional charge transport channels inside deformed diamond crystal. Results in Fig. 2(d) show that, under CS strains, the conduction-band bottom first crosses the Fermi level along the line connecting the Γ (0,0,0) and Z (0,0,0.5) points in the Brillouin zone, indicating that CS deformation created electronic conduction flows in the [001] direction along the normal compression shortened bonds. Meanwhile, hole pockets develop around the zone center. At increasing strains, as shown in Fig. 2(e) for CS strain 0.28, the electron pockets grow in size and position closer to the Z point, and the hole pockets move toward the M (0.5,0.5,0) and X (0,0.5,0) points that lie in the lateral plane. These highly directional channels suggest anisotropic electron and hole conductivity in CS strain deformed diamond.

To assess the robustness of the extraordinary structural and electronic smooth flow phenomena in CS strained diamond, we have explored a wide range of loading conditions. We adjusted the normal-to-shear stress ratio, and calculated results [Fig. 3(a)] reveal the same creeplike deformation behaviors accompanied by electronic band gap closures when the ratio is set to 2.00 and 3.00, suggesting the smooth flow in diamond is viable under a wide range of biaxial loading conditions. We also examined CS shear modes other than (11-2)[111]. Results [Fig. 3(b)] show similar smooth flow behaviors under (10-1)[111], (12-3) [111], and (22-3)[334] CS shear strains, indicating that the characteristic structural and electronic response under biaxial CS strains exist under not only multiple [111], but also similarly aligned (e.g., [334]) shear slip modes. Finally, we evaluated shear deformation of diamond under a constant large normal stress, corresponding to extreme wear loadings. Results [Fig. 3(c)] again reveal similar smooth flow behaviors. In all the cases studied, band gap closure occurs early on during the CS deformation process, creating a wide range of shear deformed diamond in metallic state (see Fig. S4 [19] for details). These assessments demonstrate that CS-driven atomistic ductility and electronic conductivity is a robust phenomenon in diamond under a diverse type and range of loading

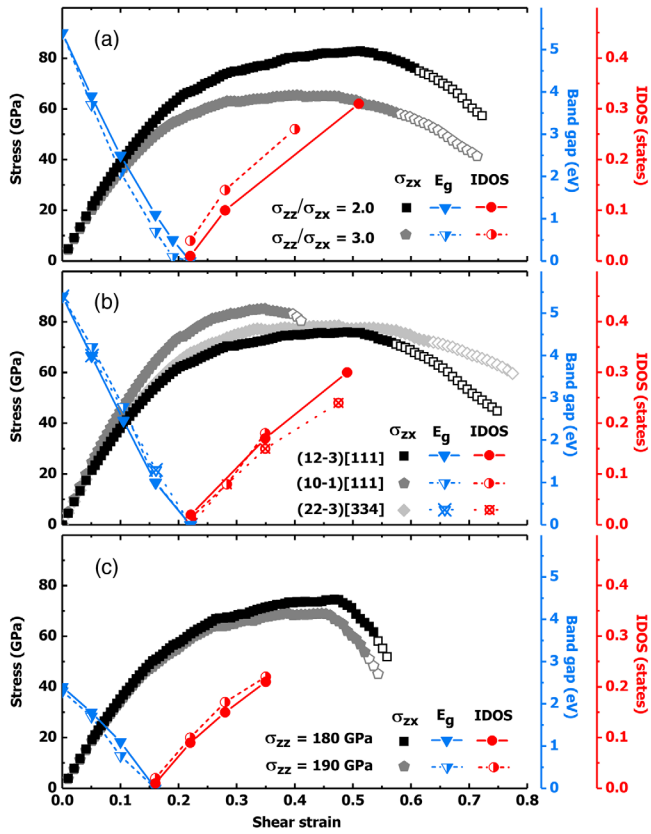


FIG. 3. Robustness of smooth structural and charge flow in diamond under CS loadings. Stress data in open symbols indicate dynamic instability revealed by imaginary phonon modes (see Fig. S3 [19] for details). (a) Creeplike smooth-flow stress responses of diamond under (11-2)[111] CS strains with a normal-to-shear stress ratio of 2.00 and 3.00, and the associated electronic band gap closure and rising IDOS, similar to those shown in Fig. 2(a). (b) Similar smooth-flow stress, band gap and IDOS behaviors under (12-3)[111], (10-1)[111], and (22-3)[334] Vickers CS strains. (c) Similar smooth-flow stress, band gap and IDOS behaviors under (11-2)[111] CS strains at fixed normal stress (180 and 190 GPa).

conditions. The essential role of the normal stress is to prevent the graphitization process usually occurring under simple tensile or shear strains. Exact normal-to-shear stress ratios or specific forms of the normal stress are not crucial, as long as graphitization is suppressed to allow CS deformation to proceed.

Our results challenge the long established paradigm on bonding and mechanical characters of diamond, and introduce unprecedented structural deformation modes and stress and charge responses under a distinct and broad class of constrained shear loading conditions. A prominent scenario concerns loaded diamond anvil cell (DAC), in which structural instability usually initiates in a small region above anvil tip where the highest stresses with large compressive and shear components appear [32,33]; coexisting extreme compressive and shear stresses also exist in the anvil culet region [34]. Smooth structural and

electronic flow could conceivably occur in these small regions, while the majority of the less strained DAC remains gapped and transparent. Such a scenario would greatly impact DAC behavior and operation, as metallization of DAC tip and culet regions would impede optical probes, and creeplike plastic flow would compromise DAC stability. Hitherto, there has been no report on experimental observation of smooth plastic flow or undoped metallic state in diamond. However, detecting the predicted soft-and-conducting modes in diamond are well within current experimental capabilities for rational experimental investigations, especially in nanoscale specimens that are nearly defect free and exhibit strains and stresses approaching theoretical limits [35,36]. Moreover, stress-strain curves and ultimate stresses and strains for diamond under complex loading are part of the nonlinear elasticity rule which is necessary for simulation and understanding of the processes in DAC, and their effect is crucial [1,2]. Another notable case is that of Robert C. DeVries which observed unusual plastic deformation of diamond under extreme wear with coexisting large compressive and shear stresses, assisted by moderate temperatures, and coined the term “work-hardening of diamond” without elucidating the underlying mechanism [37]. Our findings indicate that such wear conditions may promote smooth plastic flow to facilitate plastic shear deformation. These cases show that well controlled indentation and wear may open effective avenues for exploring novel structural flow phenomena and associated electronic properties in a variety of diamond specimens once brittle fracture modes are hindered by proper constraining compressive stress. It is noted that similar plateaus in the stress-strain curves [3–5] and metallization [5] have been seen in other covalent crystals due to elastic lattice instability caused by zero elastic moduli in the loading direction before phonon instability sets in.

The present findings offer powerful insights and guidance for experimental exploration of the predicted novel behaviors in diamond, and may also prompt reexaminations of previously encountered but unexplained phenomena. The distinct mechanisms for diamond’s unusual structural and electronic evolutions add new ingredients into modeling and simulating structural responses and elucidating resulting mechanical and electronic properties of diamond under diverse constrained shear strains by connecting to measurement details [35,36,38–40]. The newly identified constrained shear deformation proceeds through anomalously large bond-angle variations, and this distinct mechanism is in sharp contrast to previously known brittle fracture modes dominated by bond elongation with much smaller angular change or defect mediated processes via bonding variations in the vicinity of defect sites, which are all restricted to much smaller strain ranges. These robust material phenomena and favorable probing conditions make the smooth flow phenomena accessible to experimental

verification and characterization and raise exciting prospects of discovering such exceptional behaviors in other strong covalent solids. Our discovery defines diamond's new benchmark properties that have broad implications for materials research, and our findings may open new areas of research on complex strain driven phenomena in a large variety of technologically important covalent materials like silicon, germanium, and silicon carbides, among others.

This research was supported by the National Key Research and Development Program of China under Grant No. 2018YFA0703404, the Natural Science Foundation of China under Grants No. 11622432, No. 11474125, and No. 11534003, and the Program for the JLU Science and Technology Innovative Research Team.

^{*}liquan777@calypso.cn

[†]chen@physics.unlv.edu

- [1] D. Roundy, C. R. Krenn, M. L. Cohen, and J. W. Morris, Jr., Ideal Shear Strengths of fcc Aluminum and Copper, *Phys. Rev. Lett.* **82**, 2713 (1999).
- [2] J. W. Morris, Jr. and C. R. Krenn, The internal stability of an elastic solid, *Philos. Mag. A* **80**, 2827 (2000).
- [3] R. H. Telling, C. J. Pickard, M. C. Payne, and J. E. Field, Theoretical Strength and Cleavage of Diamond, *Phys. Rev. Lett.* **84**, 5160 (2000).
- [4] H. Chacham and L. Kleinman, Instabilities in Diamond under High Shear Stress, *Phys. Rev. Lett.* **85**, 4904 (2000).
- [5] S. H. Jhi, S. G. Louie, M. L. Cohen, and J. W. Morris, Jr., Mechanical Instability and Ideal Shear Strength of Transition Metal Carbides and Nitrides, *Phys. Rev. Lett.* **87**, 075503 (2001).
- [6] S. Ogata, J. Li, and S. Yip, Ideal pure shear strength of aluminum and copper, *Science* **298**, 807 (2002).
- [7] D. M. Clatterbuck, C. R. Krenn, M. L. Cohen, and J. W. Morris, Jr., Phonon Instabilities and the Ideal Strength of Aluminum, *Phys. Rev. Lett.* **91**, 135501 (2003).
- [8] S. Ogata, J. Li, N. Hirosaki, Y. Shibutani, and S. Yip, Ideal shear strain of metals and ceramics, *Phys. Rev. B* **70**, 104104 (2004).
- [9] X. Blase, P. Gillet, A. San Miguel, and P. Melinon, Exceptional Ideal Strength of Carbon Clathrates, *Phys. Rev. Lett.* **92**, 215505 (2004).
- [10] Y. Zhang, H. Sun, and C. F. Chen, Superhard Cubic BC₂N Compared to Diamond, *Phys. Rev. Lett.* **93**, 195504 (2004).
- [11] Y. Zhang, H. Sun, and C. F. Chen, Atomistic Deformation Modes in Strong Covalent Solids, *Phys. Rev. Lett.* **94**, 145505 (2005).
- [12] Y. Zhang, H. Sun, and C. Chen, Structural deformation, strength, and instability of cubic BN compared to diamond: A first-principles study, *Phys. Rev. B* **73**, 144115 (2006).
- [13] M. G. Fytas, I. N. Remediakis, P. C. Kelires, and D. A. Papaconstantopoulos, Insights into the Fracture Mechanisms and Strength of Amorphous and Nanocomposite Carbon, *Phys. Rev. Lett.* **96**, 185503 (2006).
- [14] R. F. Zhang, S. Veprek, and A. S. Argon, Anisotropic ideal strengths and chemical bonding of Wurtzite BN in comparison to Zincblende BN, *Phys. Rev. B* **77**, 172103 (2008).
- [15] D. M. Clatterbuck, D. C. Chrzan, and J. W. Morris, Jr., The influence of triaxial stress on the ideal tensile strength of iron, *Scr. Mater.* **49**, 1007 (2003).
- [16] B. Li, H. Sun, and C. F. Chen, Large indentation strain-stiffening in nanotwinned cubic boron nitride, *Nat. Commun.* **5**, 4965 (2014).
- [17] B. Li, H. Sun, and C. F. Chen, Extreme Mechanics of Probing the Ultimate Strength of Nanotwinned Diamond, *Phys. Rev. Lett.* **117**, 116103 (2016).
- [18] C. Lu, Q. Li, Y. M. Ma, and C. F. Chen, Extraordinary Indentation Strain Stiffening Produces Superhard Tungsten Nitrides, *Phys. Rev. Lett.* **119**, 115503 (2017).
- [19] See Supplemental Material at <http://link.aps.org/supplemental/10.1103/PhysRevLett.123.195504> for details on computational methods and supporting information on phonon dispersion, bond-charge variation, electronic density of states of diamond under various constrained strains, and all raw data on stress response of diamond under various strains shown in Figs. 1 and 3, which includes Refs. [20–26].
- [20] G. Kresse and J. Furthmüller, Efficient iterative schemes for ab initio total-energy calculations using a plane-wave basis set, *Phys. Rev. B* **54**, 11169 (1996).
- [21] G. Kresse and D. Joubert, From ultrasoft pseudopotentials to the projector augmented-wave method, *Phys. Rev. B* **59**, 1758 (1999).
- [22] D. M. Ceperley and B. J. Alder, Ground State of the Electron Gas by a Stochastic Method, *Phys. Rev. Lett.* **45**, 566 (1980).
- [23] H. J. Monkhorst and J. D. Pack, Special points for Brillouin-zone integrations, *Phys. Rev. B* **13**, 5188 (1976).
- [24] A. Togo, F. Oba, and I. Tanaka, First-principles calculations of the ferroelastic transition between rutile-type and CaCl₂-type SiO₂ at high pressures, *Phys. Rev. B* **78**, 134106 (2008).
- [25] J. Heyd, G. E. Scuseria, and M. Ernzerhof, Hybrid functionals based on a screened coulomb potential, *J. Chem. Phys.* **118**, 8207 (2003).
- [26] J. Heyd, G. E. Scuseria, and M. Ernzerhof, Erratum: Hybrid functionals based on a screened coulomb potential, *J. Chem. Phys.* **124**, 219906 (2006).
- [27] Y. Tian, B. Xu, D. Yu, Y. Ma, Y. Wang, Y. Jiang, W. Hu, C. Tang, Y. Gao, K. Luo, Z. Zhao, L. M. Wang, B. Wen, J. He, and Z. Liu, Ultrahard nanotwinned cubic boron nitride, *Nature (London)* **493**, 385 (2013).
- [28] Q. Huang, D. Yu, B. Xu, W. Hu, Y. Ma, Y. Wang, Z. Zhao, B. Wen, J. He, Z. Liu, and Y. Tian, Nanotwinned diamond with unprecedented hardness and stability, *Nature (London)* **510**, 250 (2014).
- [29] Z. C. Pan, H. Sun, and C. F. Chen, Colossal Shear-Strength Enhancement of Low-Density Cubic BC₂N by Nanoindentation, *Phys. Rev. Lett.* **98**, 135505 (2007).
- [30] Z. Pan, H. Sun, Y. Zhang, and C. Chen, Harder than Diamond: Superior Indentation Strength of Wurtzite BN and Lonsdaleite, *Phys. Rev. Lett.* **102**, 055503 (2009).
- [31] M. P. Surh, S. G. Louie, and M. L. Cohen, Band gaps of diamond under anisotropic stress, *Phys. Rev. B* **45**, 8239 (1992).
- [32] R. J. Hemley, H. K. Mao, G. Shen, J. Badro, P. Gillet, M. Hanfland, and D. Häusermann, X-ray imaging of stress and

- strain of diamond, iron, and tungsten at megabar pressures, *Science* **276**, 1242 (1997).
- [33] B. Li, C. Ji, W. Yang, J. Wang, K. Yang, R. Xu, W. Liu, Z. Cai, J. Chen, and H. K. Mao, Diamond anvil cell behavior up to 4 Mbar, *Proc. Natl. Acad. Sci. U.S.A.* **115**, 1713 (2018).
- [34] T. B. Shiell, D. G. McGulloch, J. E. Bradley, B. Haberl, R. Boehler, and D. R. McKenzie, Nanocrystalline hexagonal diamond formed from glassy carbon, *Sci. Rep.* **6**, 37232 (2016).
- [35] C. R. Krenn, D. Roundy, M. L. Cohen, D. C. Chrzan, and J. W. Morris, Jr., Connecting atomistic and experimental estimates of ideal strength, *Phys. Rev. B* **65**, 134111 (2002).
- [36] A. Banerjee, D. Bernoulli, H. Zhang, M. F. Yuen, J. Liu, J. Dong, F. Ding, J. Lu, M. Dao, W. Zhang, Y. Lu, and S. Suresh, Ultralarge elastic deformation of nanoscale diamond, *Science* **360**, 300 (2018).
- [37] R. C. DeVries, Plastic deformation and “work-hardening” of diamond, *Mater. Res. Bull.* **10**, 1193 (1975).
- [38] M. I. Eremets, I. A. Trojan, P. Gwaze, J. Huth, R. Boehler, and V. D. Blank, The strength of diamond, *Appl. Phys. Lett.* **87**, 141902 (2005).
- [39] T. Li, J. W. Morris, Jr., N. Nagasako, S. Kuramoto, and D. C. Chrzan, Ideal Engineering Alloys, *Phys. Rev. Lett.* **98**, 105503 (2007).
- [40] H. Wu, X. Luo, L. Wen, H. Sun, and C. F. Chen, Extreme static compression of carbon to terapascal pressures, *Carbon* **144**, 161 (2019).

Supplemental Material on Smooth Flow in Diamond: Atomistic Ductility and Electronic Conductivity

Chang Liu,¹ Xianqi Song,¹ Quan Li,^{1,2} Yanming Ma,^{1,2} and Changfeng Chen³

¹*State Key Laboratory of Superhard Materials, Key Laboratory of Automobile Materials of MOE, Department of Materials Science, and Innovation Center for Computational Physics Method and Software, Jilin University, Changchun 130012, China*

²*International Center of Future Science, Jilin University, Changchun 130012, China*

³*Department of Physics and Astronomy, University of Nevada, Las Vegas, Nevada 89154, USA*

Here we provide a systematic description on computational methods used in the present work and additional details supporting several results presented in the main text.

COMPUTATIONAL METHODS

The first-principles energetic calculations and stress-strain relations are carried out using the VASP code [1], adopting the projector augmented wave (PAW) approach [2] with carbon valence electron configuration of $2s^22p^2$. The local density approximation (LDA) is used to describe the exchange and correlation potential between electrons as parametrized by the Ceperley and Alder functional [3]. An energy cutoff of 800 eV and a Monkhorst-Pack grid [4] with a maximum spacing of $2\pi \times 0.18 \text{ \AA}^{-1}$ are adopted, achieving an energy convergence around 1 meV per atom with residual forces and stresses less than 0.005 eV\AA^{-1} and 0.1 GPa, respectively. Phonon dispersion curves are calculated by the direct supercell method [5] using forces obtained by the Hellmann-Feynman theorem. Electronic band gap is determined using the hybrid functional of Heyd-Scuseria-Ernzerhof (HSE) [6, 7].

Stress-strain relations under diverse loading conditions are calculated under a biaxial stress state that contains a shear stress and a normal compressive stress component. This approach recovers the pure shear case in the limit of zero normal stress and simulates a variety of loading environments, including the widely used Vickers indentation [8–10]. The shape of the (deformed) unit cell and atomic relaxation are determined completely at each step by the constrained structural optimization. The starting position for each strain step is taken from the relaxed coordinates of the previous strain step to ensure the quasistatic strain path, with a strain increment of 0.01 in each of the first five steps, which are in mostly linear elastic range, and then 0.005 for each subsequent steps. At each step, the applied shear strain is fixed to determine the shear stress σ_{xz} , while the other five independent components of the strain tensors and all the atoms inside the unit cell are simultaneously relaxed until the compressive stress component (σ_{zz}) reaches a specified value, namely $\sigma_{zz} = \sigma_{xz}\tan\phi$ or $\sigma_{zz} = c$, where ϕ is the centerline-to-face angle of the indenter and c is a constant normal compressive stress. We set $\tan\phi = 2.475$, 2.000 and 3.000 in the calculations, with the first value corresponds to $\phi = 68.0^\circ$, which describes the standard

Vickers indenter, while the latter two simulate general complex strain and stress states in the deformed crystal. We also set $\sigma_{zz} = 180$ and 190 GPa, with both σ_{zz} and σ_{xz} obtained independently for a given set of ϵ_{zz} and ϵ_{xz} , to simulate loading with a constant normal stress σ_{zz} as shear strain ϵ_{xz} increases. Meanwhile, all other four components of the Hellmann-Feynman stress tensor and the force on each atom become negligibly small, typically less than 0.1 GPa and 0.005 eV\AA^{-1} , respectively.

-
- [1] G. Kresse and L. Furthmüller, Efficient Iterative Schemes for Ab initio Total-Energy Calculations Using a Plane-Wave Basis Set. *Phys. Rev. B* **54**, 11169 (1996).
 - [2] G. Kresse and D. Joubert, From Ultrasoft Pseudopotentials to the Projector Augmented-Wave Method. *Phys. Rev. B* **59**, 1758 (1999).
 - [3] D. M. Ceperley and B. J. Alder, Ground State of the Electron Gas by a Stochastic Method. *Phys. Rev. Lett.* **45**, 566 (1980).
 - [4] H. J. Monkhorst and J. D. Pack, Special Points for Brillouin-Zone Integrations. *Phys. Rev. B* **13**, 5188 (1976).
 - [5] A. Togo, F. Oba, and I. Tanaka, First-principles calculations of the ferroelastic transition between rutile-type and CaCl_2 -type SiO_2 at high pressures. *Phys. Rev. B* **78**, 134106 (2008).
 - [6] J. Heyd, G. E. Scuseria, and M. Ernzerhof, Hybrid Functionals Based on a Screened Coulomb Potential. *J. Chem. Phys.* **118**, 8207 (2003).
 - [7] J. Heyd, G. E. Scuseria, and M. Ernzerhof, Erratum: Hybrid Functionals Based on a Screened Coulomb Potential. *J. Chem. Phys.* **124**, 219906 (2006).
 - [8] Z. C. Pan, H. Sun, and C. F. Chen, Colossal shear-strength enhancement of lowdensity cubic BC_2N by nanoindentation. *Phys. Rev. Lett.* **98**, 135505 (2007).
 - [9] Z. C. Pan, H. Sun, Y. Zhang, and C. F. Chen, Harder than diamond: superior indentation strength of wurtzite BN and lonsdaleite. *Phys. Rev. Lett.* **102**, 105503 (2009).
 - [10] B. Li, H. Sun, and C. F. Chen, Large indentation strain stiffening in nanotwinned cubic boron nitride. *Nat. Commun.* **5**, 4965 (2014).

TABLE S1: Raw data on stress response of diamond under CS (with a normal to shear ratio of 2.475) or PS (111)[11-2] strains shown in Fig. 1(a).

CS		PS	
ϵ_{xz}	σ_{xz} (GPa)	ϵ_{xz}	σ_{xz} (GPa)
0.000	0.0	0.000	0.0
0.010	4.5	0.010	5.1
0.020	9.0	0.020	10.1
0.030	13.1	0.030	15.0
0.041	17.1	0.041	19.8
0.051	21.1	0.051	24.6
0.056	23.0	0.062	29.3
0.062	24.8	0.072	33.9
0.067	26.7	0.083	38.4
0.072	28.5	0.094	42.9
0.078	30.2	0.105	47.2
0.083	32.0	0.116	51.5
0.088	33.7	0.127	55.6
0.094	35.3	0.138	59.7
0.099	37.0	0.149	63.6
0.105	38.6	0.161	67.4
0.110	40.1	0.173	71.1
0.116	41.7	0.184	74.7
0.121	43.2	0.196	78.1
0.127	44.7	0.208	81.3
0.133	46.1	0.220	84.3
0.138	47.6	0.232	87.1
0.144	49.0	0.245	89.5
0.150	50.3	0.257	91.7
0.155	51.7	0.270	93.4
0.161	53.0	0.282	94.5
0.167	54.2	-	-
0.173	55.3	-	-
0.179	56.5	-	-
0.185	57.6	-	-
0.191	58.6	-	-
0.197	59.7	-	-
0.203	60.6	-	-
0.209	60.8	-	-
0.215	61.7	-	-
0.221	62.4	-	-
0.227	62.8	-	-
0.233	63.6	-	-
0.239	64.2	-	-
0.245	64.6	-	-
0.251	65.4	-	-
0.258	66.2	-	-
0.264	66.9	-	-
0.270	67.2	-	-
0.277	67.9	-	-
0.283	68.5	-	-
0.289	68.7	-	-
0.296	68.8	-	-
0.302	68.9	-	-
0.309	69.2	-	-
0.315	69.4	-	-
0.322	69.8	-	-
0.329	69.9	-	-
0.335	70.3	-	-
0.342	70.2	-	-
0.349	70.5	-	-

CS		PS	
ϵ_{xz}	σ_{xz} (GPa)	ϵ_{xz}	σ_{xz} (GPa)
0.355	71.1	-	-
0.362	71.6	-	-
0.369	71.8	-	-
0.376	72.2	-	-
0.383	72.2	-	-
0.390	72.6	-	-
0.397	72.6	-	-
0.404	72.9	-	-
0.411	72.6	-	-
0.418	72.8	-	-
0.425	73.1	-	-
0.432	72.8	-	-
0.439	72.8	-	-
0.446	72.8	-	-
0.453	72.9	-	-
0.461	72.9	-	-
0.468	73.1	-	-
0.475	73.4	-	-
0.483	73.5	-	-
0.490	73.4	-	-
0.498	72.9	-	-
0.505	72.2	-	-
0.513	72.3	-	-
0.520	71.9	-	-
0.528	70.9	-	-
0.535	70.1	-	-
0.543	69.7	-	-
0.551	69.4	-	-
0.559	69.1	-	-
0.566	68.7	-	-
0.574	68.0	-	-
0.582	67.2	-	-
0.590	66.4	-	-

TABLE S2: Raw data on stress response of diamond under CS (111)[11-2] strains with a normal to shear ratio of 2.0 or 3.0 shown in Fig. 3(a).

$\sigma_{zz}/\sigma_{xz} = 2.0$			$\sigma_{zz}/\sigma_{xz} = 3.0$		
ϵ_{xz}	σ_{xz} (GPa)	σ_{xz} (GPa)	ϵ_{xz}	σ_{xz} (GPa)	σ_{xz} (GPa)
0.000	0.0	0.0	0.362	78.0	64.7
0.010	4.8	4.4	0.369	78.7	64.9
0.020	9.2	8.7	0.376	79.3	64.9
0.030	13.5	12.7	0.383	79.8	65.1
0.041	17.7	16.5	0.390	80.3	65.3
0.051	21.8	20.3	0.397	80.3	65.3
0.056	23.8	22.1	0.404	80.7	65.4
0.062	25.7	23.9	0.411	80.8	65.3
0.067	27.7	25.6	0.418	80.5	64.8
0.072	29.6	27.3	0.425	81.0	64.9
0.078	31.4	29.0	0.432	81.3	65.1
0.083	33.3	30.6	0.439	81.7	65.0
0.088	35.1	32.2	0.446	81.9	65.1
0.094	36.9	33.7	0.453	82.2	65.1
0.099	38.6	35.2	0.461	82.0	65.0
0.105	40.3	36.7	0.468	82.0	65.1
0.110	42.0	38.2	0.475	82.2	64.9
0.116	43.7	39.6	0.483	82.2	64.3
0.121	45.3	41.0	0.490	82.5	63.9
0.127	46.9	42.4	0.498	82.7	63.7
0.133	48.5	43.7	0.505	82.8	63.4
0.138	50.0	45.0	0.513	82.9	62.7
0.144	51.6	46.3	0.520	82.5	61.9
0.150	53.0	47.5	0.528	82.3	61.5
0.155	54.5	48.7	0.535	82.1	61.3
0.161	55.9	49.9	0.543	81.0	60.8
0.167	57.4	50.9	0.551	80.9	60.4
0.173	58.7	52.0	0.559	80.6	59.9
0.179	60.0	53.0	0.566	79.8	59.2
0.185	61.1	53.9	0.574	79.2	58.6
0.191	62.4	54.8	0.582	78.7	-
0.197	63.5	55.2	0.590	77.9	-
0.203	64.6	55.9			
0.209	65.7	56.5			
0.215	66.4	57.3			
0.221	66.8	57.8			
0.227	67.4	58.2			
0.233	68.0	58.6			
0.239	69.0	59.4			
0.245	70.0	60.1			
0.251	70.4	60.6			
0.258	71.1	61.0			
0.264	71.9	61.5			
0.270	72.8	62.1			
0.277	73.5	62.5			
0.283	74.1	63.1			
0.289	74.6	63.0			
0.296	74.9	63.0			
0.302	75.0	62.8			
0.309	75.2	63.0			
0.315	75.7	63.3			
0.322	76.2	63.5			
0.329	76.4	63.8			
0.335	76.9	63.9			
0.342	77.1	64.1			
0.349	77.2	64.0			
0.355	77.8	64.3			

$\sigma_{zz}/\sigma_{xz} = 2.0$			$\sigma_{zz}/\sigma_{xz} = 3.0$		
ϵ_{xz}	σ_{xz} (GPa)	σ_{xz} (GPa)	ϵ_{xz}	σ_{xz} (GPa)	σ_{xz} (GPa)
0.362	78.0	64.7	0.369	78.7	64.9
0.376	79.3	64.9	0.383	79.8	65.1
0.390	80.3	65.3	0.397	80.3	65.3
0.404	80.7	65.4	0.411	80.8	65.3
0.418	80.5	64.8	0.425	81.0	64.9
0.432	81.3	65.1	0.439	81.7	65.0
0.446	81.9	65.1	0.453	82.2	65.1
0.461	82.0	65.0	0.468	82.0	65.1
0.475	82.2	64.9	0.483	82.2	64.3
0.490	82.5	63.9	0.498	82.7	63.7
0.505	82.8	63.4	0.513	82.9	62.7
0.520	82.5	61.9	0.528	82.3	61.5
0.535	82.1	61.3	0.543	81.0	60.8
0.551	80.9	60.4	0.559	80.6	59.9
0.566	79.8	59.2	0.574	79.2	58.6
0.582	78.7	-	0.590	77.9	-

TABLE S3: Raw data on stress response of diamond under (12-3)[111], (10-1)[111], or (22-3)[334] Vickers CS strains shown in Fig. 3(b).

	(12-3)[111]	(10-1)[111]	(22-3)[334]
ϵ_{xz}	σ_{xz} (GPa)	σ_{xz} (GPa)	σ_{xz} (GPa)
0.000	0.0	0.0	0.0
0.010	4.6	5.1	4.6
0.020	9.1	10.2	9.2
0.030	13.4	15.1	13.6
0.041	17.5	20.0	17.9
0.051	21.6	24.8	22.1
0.056	23.5	27.1	24.1
0.062	25.4	29.4	26.1
0.067	27.3	31.6	28.1
0.072	29.2	33.9	30.0
0.078	31.0	36.1	31.9
0.083	32.8	38.2	33.8
0.088	34.5	40.4	35.6
0.094	36.3	42.5	37.4
0.099	37.9	44.5	39.2
0.105	39.6	46.6	40.9
0.110	41.2	48.6	42.6
0.116	42.8	50.5	44.2
0.121	44.4	52.4	45.8
0.127	45.9	54.3	47.4
0.133	47.4	56.2	49.0
0.138	48.9	58.0	50.5
0.144	50.3	59.7	52.0
0.150	51.7	61.4	53.5
0.155	53.1	63.1	54.9
0.161	54.5	64.7	56.3
0.167	55.8	66.2	57.6
0.173	56.8	67.7	59.0
0.179	58.1	69.0	60.3
0.185	59.3	70.5	61.5
0.191	60.3	71.9	62.7
0.197	61.4	73.3	63.7
0.203	62.3	74.1	64.8
0.209	62.8	74.3	65.9
0.215	63.4	75.2	66.9
0.221	63.9	76.2	67.8
0.227	64.5	77.2	68.3
0.233	65.3	78.2	68.8
0.239	66.0	78.9	69.7
0.245	66.7	79.8	70.3
0.251	67.2	80.4	71.0
0.258	68.0	81.3	71.5
0.264	68.7	81.6	71.8
0.270	69.4	81.9	72.4
0.277	69.9	82.3	72.9
0.283	70.5	82.7	73.7
0.289	70.5	83.2	74.2
0.296	70.5	83.1	74.8
0.302	70.9	83.5	75.3
0.309	71.3	83.8	75.6
0.315	71.4	84.2	76.1
0.322	71.7	84.7	76.5
0.329	71.8	84.7	77.0
0.335	72.3	85.0	77.2
0.342	72.4	85.1	77.1
0.349	72.8	85.2	76.8
0.355	73.1	84.5	76.5

	(12-3)[111]	(10-1)[111]	(22-3)[334]
ϵ_{xz}	σ_{xz} (GPa)	σ_{xz} (GPa)	σ_{xz} (GPa)
0.362	73.5	84.3	76.9
0.369	74.0	84.1	77.0
0.376	74.4	83.8	77.5
0.383	74.6	83.5	77.6
0.390	74.6	83.3	77.5
0.397	74.9	-	77.3
0.404	75.0	-	77.2
0.411	74.7	-	77.5
0.418	75.1	-	78.0
0.425	75.2	-	78.0
0.432	75.4	-	78.2
0.439	75.7	-	78.1
0.446	75.8	-	78.1
0.453	75.5	-	78.1
0.461	75.4	-	78.3
0.468	75.7	-	78.4
0.475	75.8	-	78.5
0.483	75.9	-	77.7
0.490	76.0	-	77.4
0.498	75.8	-	77.3
0.505	75.8	-	77.3
0.513	75.7	-	77.5
0.520	75.1	-	77.5
0.528	74.7	-	77.5
0.535	74.3	-	77.5
0.543	73.3	-	77.3
0.551	72.9	-	77.2
0.559	72.5	-	77.0
0.566	72.0	-	76.6
0.574	-	-	76.6
0.582	-	-	75.9
0.590	-	-	75.4
0.598	-	-	74.9
0.606	-	-	73.8
0.614	-	-	73.2
0.622	-	-	72.7
0.630	-	-	72.4

TABLE S4: Raw data on stress response of diamond under CS strains at a fixed normal stress of 180 or 190 GPa shown in Fig. 3(c).

$\sigma_{zz} = 180 \text{ GPa}$		$\sigma_{zz} = 190 \text{ GPa}$	
ϵ_{xz}	σ_{xz} (GPa)	ϵ_{xz}	σ_{xz} (GPa)
0.000	0.0	0.0	
0.010	4.0	3.8	
0.020	7.9	7.6	
0.030	11.8	11.4	
0.041	15.5	15.1	
0.051	19.3	18.7	
0.056	21.1	20.6	
0.062	22.9	22.3	
0.067	24.8	24.1	
0.072	26.5	25.8	
0.078	28.3	27.7	
0.083	30.1	29.3	
0.088	31.8	31.0	
0.094	33.5	32.7	
0.099	35.2	34.1	
0.105	37.0	35.8	
0.110	38.5	37.4	
0.116	40.0	39.0	
0.121	41.6	40.6	
0.127	43.2	42.0	
0.133	44.7	43.4	
0.138	46.1	44.9	
0.144	47.6	46.2	
0.150	49.0	47.2	
0.155	50.3	48.0	
0.161	51.0	49.2	
0.167	52.0	50.1	
0.173	53.0	51.3	
0.179	54.3	52.5	
0.185	55.4	53.2	
0.191	56.6	54.1	
0.197	57.1	54.8	
0.203	57.8	55.9	
0.209	58.8	57.1	
0.215	59.9	57.9	
0.221	61.0	59.1	
0.227	61.8	60.0	
0.233	62.8	60.6	
0.239	63.5	61.5	
0.245	64.3	62.2	
0.251	65.2	63.0	
0.258	66.0	63.8	
0.264	66.9	64.4	
0.270	67.2	64.0	
0.277	67.2	64.0	
0.283	67.7	64.1	
0.289	67.4	64.8	
0.296	67.9	64.9	
0.302	68.6	65.6	
0.309	68.9	66.0	
0.315	68.8	66.2	
0.322	69.5	66.3	
0.329	70.1	66.1	
0.335	70.7	66.6	
0.342	71.0	67.3	
0.349	71.4	67.6	
0.355	71.8	67.9	

$\sigma_{zz} = 180 \text{ GPa}$		$\sigma_{zz} = 190 \text{ GPa}$	
ϵ_{xz}	σ_{xz} (GPa)	ϵ_{xz}	σ_{xz} (GPa)
0.362	72.1		68.1
0.369	72.6		68.5
0.376	72.6		68.6
0.383	73.0		69.1
0.390	73.5		69.0
0.397	73.2		68.4
0.404	73.7		68.5
0.411	73.4		68.6
0.418	73.8		68.5
0.425	73.5		68.6
0.432	73.7		68.8
0.439	73.5		68.9
0.446	73.8		69.0
0.453	74.4		68.9
0.461	74.4		68.3
0.468	74.6		66.8
0.475	74.4		65.9
0.483	73.2		64.9
0.490	72.3		62.1
0.498	71.3		60.3
0.505	68.8		59.0
0.513	66.9		56.9
0.520	65.4		53.8
0.528	63.9		-
0.535	61.8		-

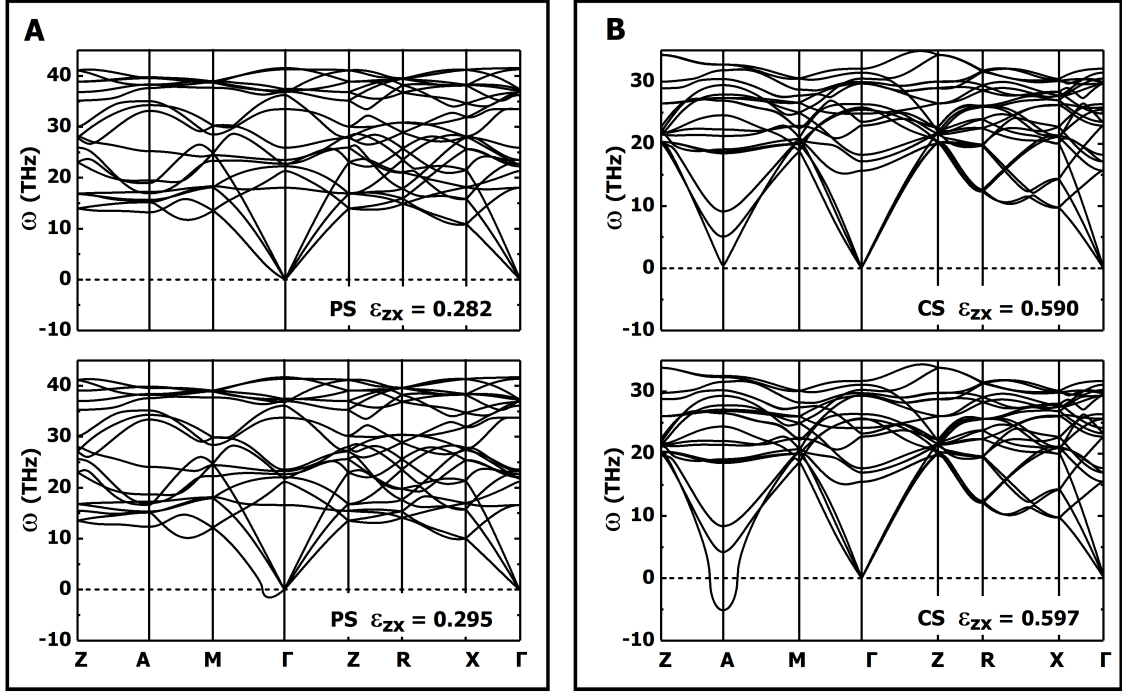


FIG. S1: Calculated phonon dispersion curves for the deformed diamond crystal under (A) pure shear (PS) and (B) constrained shear (CS) (111)[11-2] strains right before (upper panel) and after (lower panel) the appearance of imaginary phonon modes that indicate the onset of dynamic instability of the structure along the stress-strain deformation path shown in Fig. 1(A) in the main text.

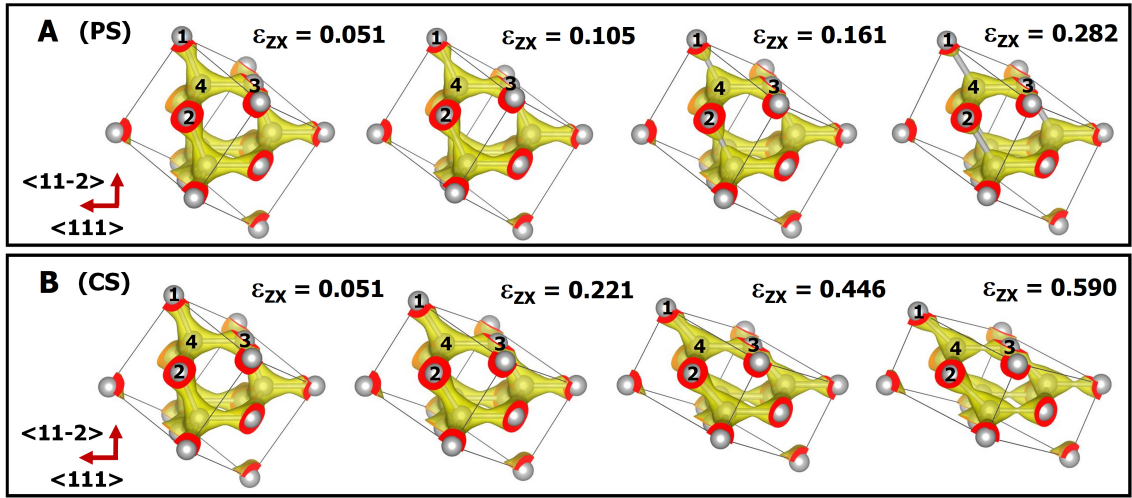


FIG. S2: An expanded view of the valence charge density (at iso-surface of 0.215 electron/bohr³) of deformed diamond crystal under (A) pure shear (PS) and (B) constrained shear (CS) (111)[11-2] strains, illustrating more detailed evolution patterns of bonding charge concentrations that determine the strengths of distinct key load-bearing bonds in each case as presented in Fig. 1(E) in the main text.

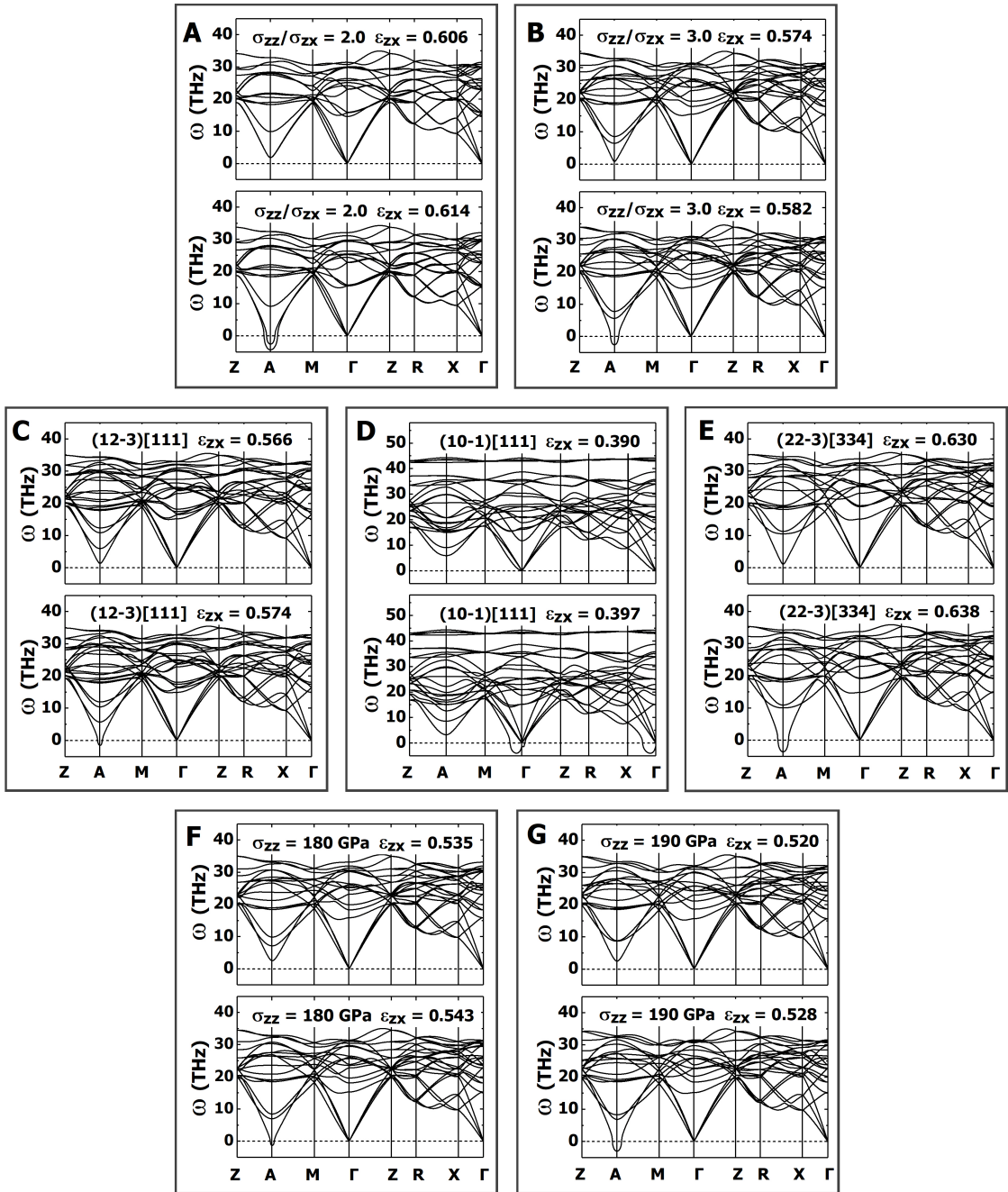


FIG. S3: Calculated phonon dispersion curves for the deformed diamond crystal under various constrained shear strains right before (upper panel) and after (lower panel) the appearance of imaginary phonon modes that indicate the onset of dynamic instability of the structure when deformed along the stress-strain curves shown in Fig. 3 in the main text. (A,B) Deformation under (11-2)[111] CS strains with a normal-to-shear stress ratio of 2.00 and 3.00. (C-E) Deformation under (12-3)[111], (10-1)[111] and (22-3)[334] CS strains. (F,G) Deformation under (11-2)[111] CS strains at fixed normal stress (180 and 190 GPa).

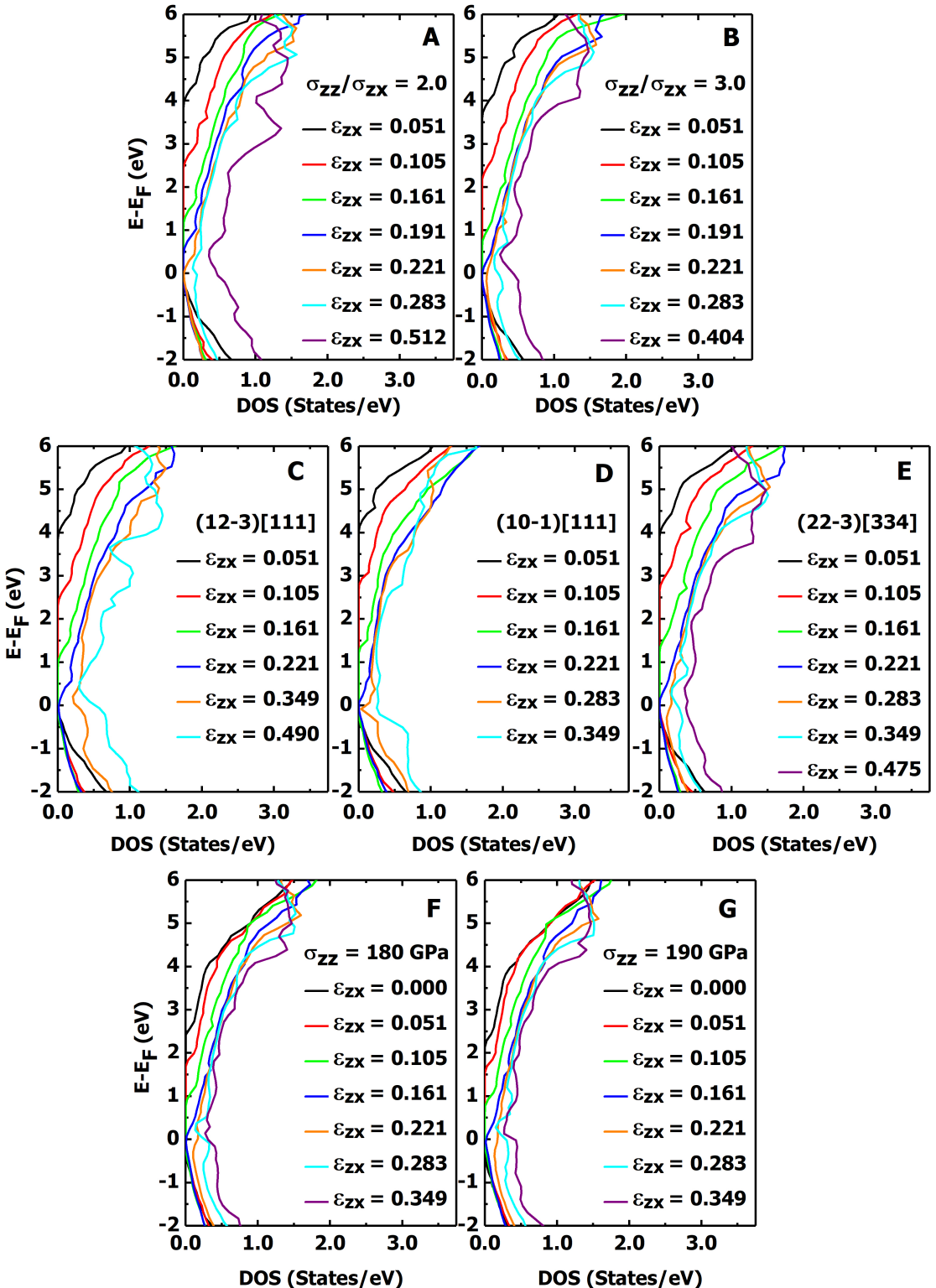


FIG. S4: Calculated electronic density of states of the deformed diamond crystal under various constrained shear strains when deformed along the stress-strain curves shown in Fig. 3 in the main text, at the same conditions listed in Fig. 3 and also in the caption of Fig. S3 above.